Thermodynamics of protein destabilization in live cells

Jens Danielsson[a,1,2], Xin Mu[a,1], Lisa Lang[a], Huabing Wang[a], Andres Binolfi[b], François-Xavier Theillet[b], Beata Bekei[b], Derek T. Logan[c], Philipp Selenko[b], Håkan Wennerström[d], and Mikael Oliveberg[a,2]

[a]Department of Biochemistry and Biophysics, Arrhenius Laboratories of Natural Sciences, Stockholm University, 10691 Stockholm, Sweden; [b]In-Cell Nuclear Magnetic Resonance (NMR) Laboratory, Department of NMR-Supported Structural Biology, Leibniz Institute of Molecular Pharmacology (FMP Berlin), 13125 Berlin, Germany; [c]Division of Biochemistry and Structural Biology, Department of Chemistry, Lund University, 22100 Lund, Sweden; and [d]Division of Physical Chemistry, Department of Chemistry, Lund University, 22100 Lund, Sweden

Edited by William A. Eaton, National Institute of Diabetes and Digestive and Kidney Diseases, National Institutes of Health, Bethesda, MD, and approved August 24, 2015 (received for review June 12, 2015)

Although protein folding and stability have been well explored under simplified conditions in vitro, it is yet unclear how these basic self-organization events are modulated by the crowded interior of live cells. To find out, we use here in-cell NMR to follow at atomic resolution the thermal unfolding of a β-barrel protein inside mammalian and bacterial cells. Challenging the view from in vitro crowding effects, we find that the cells destabilize the protein at 37 °C but with a conspicuous twist: While the melting temperature goes down the cold unfolding moves into the physiological regime, coupled to an augmented heat-capacity change. The effect seems induced by transient, sequence-specific, interactions with the cellular components, acting preferentially on the unfolded ensemble. This points to a model where the in vivo influence on protein behavior is case specific, determined by the individual protein's interplay with the functionally optimized "interaction landscape" of the cellular interior.

thermodynamics | protein stability | crowding | in vivo | NMR

Unlike their static impression in X-ray structures and textbook illustrations, some proteins are tuned to work at marginal structural stability. The advantage of such tuning is that it enables the protein to easily switch from one conformation to another, providing sensitive functional control. A well-known example is the tumor suppressor P53 whose function in gene regulation relies on a complex interplay of local folding–unfolding transitions (1). Likewise, the maturation pathway of the radical scavenger Cu/Zn superoxide dismutase (SOD1) involves a marginally stable apo species that seems required for interorganelle trafficking (2) and effective chaperone-assisted metal loading (3). As an inevitable consequence of such near-equilibrium action, however, the proteins become critically sensitive to perturbations (1): Mutation of SOD1 triggers with full penetrance late-onset neurodegenerative disease even though the causative mutations shift the structural equilibrium only by less than a factor of 3 (4). In the latter case, it is not the loss of native function that poses the acute problem, but rather the promotion of competing disordered SOD1 conformations that eventually exhaust the cellular proteostasis system and end up in pathologic deposits (5–8). Uncovering the rules, capacity and limitations of this delicate interplay between individual proteins and the cellular components (9, 10) requires not only information about the in vivo response to molecular perturbations, but also precise quantification of the structural equilibria at play. The question is then, to what extent are existing data obtained under simplified conditions in vitro transferable to the complex environment in live cells (11)? The answer is not clear cut. Defying predictions from steric crowding effects (11–13), experimental data have shown that cells in some cases stabilize (14–19) and in other cases destabilize (20–25) the native protein structures. In this study, we shed light on these seemingly conflicting results by mapping out the thermodynamic behavior of a marginally stable β-barrel protein ($SOD1^{barrel}$), using in-cell NMR. Our results show that mammalian and bacterial cells not only destabilize $SOD1^{barrel}$, but also render its structure essentially disordered at 37 °C. The effect is assigned to transient interactions with the cellular interior, which counterbalance the crowding pressure, narrow the width of the thermal unfolding transitions, and move both cold and heat unfolding into the physiological regime. Moreover, these transient interactions are seen to be sequence and context dependent, reconciling the previous observations that different proteins yield different results. The emerging picture is thus that proteins are optimized not only for structure and function but also for their interplay with the host-cell environment, raising interesting questions about the physiological manifestation of marginal stability, as well as the constraints on protein behavior across evolutionary diverse organisms.

Results

In-Cell Effects on the Folded State. Our model protein is the 110-residue β-barrel scaffold [Protein Data Bank (PDB) code 4BCZ] of the ubiquitous radical scavenger *Cu/Zn superoxide dismutase* (PDB code 1HL5). This SOD1 variant ($SOD1^{barrel}$) was constructed by truncating the metal-binding loop IV and the electrostatic loop VII of the mother protein (26), which obliterates the native dimerization and leaves a catalytically inactive, well-behaved monomer that presents several advantages for in-cell analysis (Fig. S1). The $SOD1^{barrel}$ displays a simplistic two-state folding transition (26); lacks complexity in form of native metal-binding ligands (27) and cysteine moieties (28); and is extensively characterized with respect to mutational response (27, 29, 30), structural dynamics (26, 31), and aggregation behavior (6). Also, $SOD1^{barrel}$ displays fully resolved NMR spectra in mammalian cells (32). For the mammalian-cell experiments, we used the

Significance

A key question in structural biology is how protein properties mapped out under simplified conditions in vitro transfer to the complex environment in live cells. The answer, it appears, varies. Defying predictions from steric crowding effects, experimental data have shown that cells in some cases stabilize and in other cases destabilize the native protein structures. In this study, we reconcile these seemingly conflicting results by showing that the in-cell effect on protein thermodynamics is sequence specific: The outcome depends both on the individual target protein and on its detailed host-cell environment.

Author contributions: J.D., X.M., H. Wang, H. Wennerström, and M.O. designed research; J.D., X.M., L.L., H. Wang, A.B., F.-X.T., B.B., D.T.L., P.S., H. Wennerström, and M.O. performed research; J.D., X.M., L.L., H. Wang, D.T.L., H. Wennerström, and M.O. analyzed data; and J.D., H. Wang, D.T.L., H. Wennerström, and M.O. wrote the paper.

The authors declare no conflict of interest.

This article is a PNAS Direct Submission.

Freely available online through the PNAS open access option.

Data deposition: The atomic coordinates and structure factors have been deposited in the Protein Data Bank, www.pdb.org (PDB code 4XCR).

[1]J.D. and X.M. contributed equally to this work.

[2]To whom correspondence may be addressed. Email: mikael.oliveberg@dbb.su.se or jens.danielsson@dbb.su.se.

This article contains supporting information online at www.pnas.org/lookup/suppl/doi:10.1073/pnas.1511308112/-/DCSupplemental.

human ovary adenocarcinoma cell line A2780 (33), which was found to have good properties for protein delivery and sustainability in the NMR tubes. ^{15}N-labeled protein was delivered into the cytosol of mammalian cells by electroporation (*SI Materials and Methods*) and after recovery and washing, the treated cells were gently packed in an NMR tube (*SI Materials and Methods*). Intracellular SOD1^{barrel} concentrations were 20–30 μM, matching those in transgenic ALS mice (34, 35), and substantially higher than the 1- to 5-μM endogenous concentration of SOD1 in mammalian cells (36). Controls of efficiency and yield of internalization are described in *SI Controls* and Fig. S2*A*. The results show high-resolution in-cell heteronuclear multiple quantum coherence (HMQC) spectra of folded and freely tumbling SOD1^{barrel} molecules, matching closely those obtained in vitro (*SI Controls* and Fig. S2*B*). A notable effect of the internalization, however, is an increased degree of protonation of the protein's histidine side chains. By using SOD1^{I35A} itself as a pH probe, we determine the intracellular pH to 6.5 (*SI Controls* and Fig. S2*C*). This cytosolic acidification is expected and arises from the hypoxic conditions in tightly packed NMR tubes: The cultured cancer cells redirect their metabolism to glycolytic pathways with little effect on viability (32). The NMR cross peaks show that the acidification commences early in the experiment, is uniform across the protein population, and remains stable for more than 5 h.

Thermodynamic Analysis. Although the in-cell spectrum of folded SOD1^{barrel} can be used for establishing the cytosolic pH and basic molecular mobility, it cannot be used on its own for measurement of the folding equilibrium. Such an analysis requires simultaneous detection of both the folded (N) and denatured (D) states in free equilibrium, i.e., an unfolding titration curve (37), where the folding equilibrium ($K_{D\text{-}N}$) and stability ($\Delta G_{D\text{-}N}$) are given by

$$\Delta G_{D\text{-}N} = -RT\ \ln K_{D\text{-}N} = \frac{-RT\ \ln[N]}{[D]}. \quad [1]$$

To establish such balanced equilibrium, we destabilized SOD1^{barrel} by the core mutation I35A (SOD1^{I35A}). The mutation leaves the structure and surface unchanged (*SI Controls*, Fig. S3 *A–F*, and Table S1) but renders the protein partly unfolded under physiological conditions. As proof of principle, the NMR spectrum of SOD1^{I35A} shows mixed populations of D and N in PBS buffer at pH 6.5 and 37 °C (Fig. 1). For quantification of $K_{D\text{-}N}$ = [N]/[D] we use the volumes of the C-terminal Q153 cross peaks, which are well separated and insensitive to temperature/viscosity-induced relaxation effects (*SI Controls* and Fig. S3 *G–L*). Upon lowering the temperature, the SOD1^{I35A} equilibrium shifts progressively toward N, displaying a thermal unfolding midpoint of T_m = 35 °C in the in vitro control (Fig. 1). At 17 °C, N reaches a maximum occupancy of 85% to finally decrease again as the temperature becomes lower still. This curved temperature dependence of $K_{D\text{-}N}$ is a generic effect of the heat-capacity increase upon unfolding (ΔC_p) according to refs. 37 and 38,

$$\Delta G_{D\text{-}N}(T) = \Delta H_{D\text{-}N}(T_0) - T\Delta S_{D\text{-}N}(T_0) + \Delta C_p\left[T - T_0 - T\ \ln\left(\frac{T}{T_0}\right)\right], \quad [2]$$

where $\Delta H_{D\text{-}N}$ and $\Delta S_{D\text{-}N}$ are the enthalpy and entropy of unfolding, respectively. The ΔC_p change is due to an increase in the hydrophobic hydration and provides a useful measure of the increase in solvent-accessible surface area of the N to D transition (39). Because the hydration grows "stronger" at lower temperatures, the larger surface area of D promotes cold unfolding and curved $\Delta G_{D\text{-}N}(T)$ profiles (38). For SOD1^{I35A}, the cold-unfolding midpoint is determined to T_C = –3 °C, in good agreement with independent controls based on CD data (*SI Controls* and Fig. S4 *A* and *B*). This thermodynamic description of SOD1^{I35A} in vitro sets the reference for quantification of the in cell effects (Table 1 and Table S2).

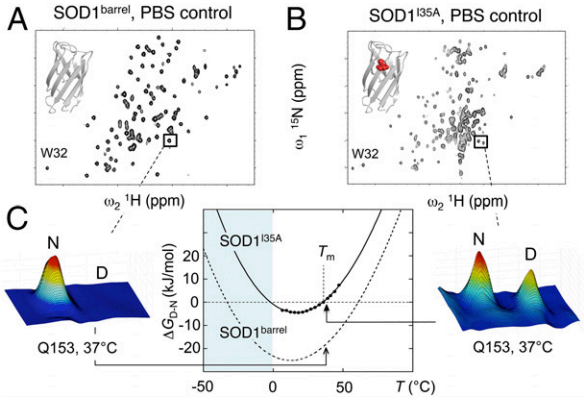

Fig. 1. In vitro benchmarking of SOD1^{barrel}, poised at marginal thermodynamic stability by the mutation SOD1^{I35A}. (*A*) HMQC spectra of SOD1^{barrel} at 37 °C, showing uniformly folded protein. *Inset* shows the X-ray structure of SOD1^{barrel} (PDB code 4BCZ), constituting the β-barrel scaffold of the parent ALS-associated protein Cu/Zn superoxide dismutase 1 (32). (*B*) Corresponding HMQC spectra of the mutant SOD1^{I35A} (PDB code 4XCR), showing mixed population of folded (N) and unfolded (D) material. Quantification of the D/N equilibrium is from the cross-peak volumes of the C-terminal resonance Q153. (*C*) $\Delta G_{D\text{-}N}$ vs. temperature profiles of SOD1^{barrel} and SOD1^{I35A} obtained from NMR thermal scans. The populations of D and N vs. temperature show melting a point T_m = 35.4 °C, i.e., $\Delta G_{D\text{-}N}$ = 0 (Eq. **1**), and cold unfolding at subzero temperature. The curved $\Delta G_{D\text{-}N}$ profiles with stability maxima around room temperature are characteristic for naturally evolved proteins (58) and define a standard set of thermodynamic parameters with well-established structural meaning (Eq. **2**).

Cells Promote Global Unfolding of SOD1^{I35A}. Upon transfer into the mammalian A2780 cells the protein SOD1^{I35A} is clearly destabilized: At 37 °C, the folding equilibrium shifts fourfold toward the denatured state (Fig. 2 and Table 1). Notably, this effect is opposite to that expected from steric crowding (11–13) and points to the presence of attractive interactions between SOD1^{I35A} and the intracellular medium. The nature of these interactions is indicated by the temperature dependence of the in-cell stability. Inside cells, the D ⇄ N transition shows a 37% increase of ΔC_p (Table S2), resulting in a narrowing of the thermal unfolding transitions (Fig. 2). Also, the D and N species remain in dynamic equilibrium during the 4-h experiments, without significant drift of populations or loss of protein material (*SI Controls* and Fig. S4*C*). Because the NMR chemical shifts and line broadening suggest that the structure of internalized N remains unchanged and free of specific interactions (Fig. S3), it is reasonable to conclude that the ΔC_p increase is mainly due to in-cell modulation of D. For controls of data skewing by temperature-induced pH shifts and ionic strength, see *SI Controls* and Fig. S4 *D–H*. As an additional test, we performed in-cell experiments on SOD1^{I35A} overexpressed in *Escherichia coli* (Fig. 2). The results show that *E. coli* decreases T_m to a smaller extent than A2780 cells, but lifts the $\Delta G_{D\text{-}N}(T)$ profile to overall lower stability (Fig. 2). Coupled to this lift is a substantial increase in the cold-unfolding midpoint, which moves into the physiological regime at T_C = 8.4 ± 1.7 °C (Table 1), and the temperature for maximum SOD1^{I35A} stability shifts from 14 °C in mammalian cells to 20 °C in *E. coli* (Fig. 2, Table 1, *SI Data*, and Fig. S5 *A*, *H*, and *I*). Thus, judging by T_m alone, the mammalian cells would deceptively appear to have a smaller destabilizing effect than *E. coli*, emphasizing the importance of characterizing the whole $\Delta G_{D\text{-}N}(T)$ profile in this type of experiment. Because of higher line broadening in *E. coli* cells (Fig. S5 *H* and *I*), we are currently unable to accurately determine $K_{D\text{-}N}$ = [N]/[D] below 10 °C and, hence, the precise effect on ΔC_p. From the ΔC_p increase in mammalian cells, however, it is indicated that the SOD1^{I35A} destabilization is here accompanied by increased surface area of the

Table 1. Thermodynamic parameters of the in-cell data and in vitro controls

Protein/conditions	$\Delta G_{D\text{-}N}$*, kJ/mol	T_m, °C	T_C†, °C
$SOD1^{barrel}$/PBS‡	−18.6 ± 0.3	61.0 ± 0.3	−33.1 ± 1.8
$SOD1^{I35A}$/PBS	0.64 ± 0.12	35.6 ± 0.3	−2.1 ± 1.4
$SOD1^{I35A}$/in A2780 cells	4.49 ± 0.50	28.0 ± 0.5	1.1 ± 0.6
$SOD1^{I35A}$/in *E. coli* cells	2.25 ± 0.30	31.0 ± 0.7	8.4 ± 1.7
$SOD1^{I35A}$/ficoll 70§	−0.62 ± 0.14	38.5 ± 0.4	−7.8 ± 1.7
$SOD1^{I35A}$/PEG^{400}§	−0.39 ± 0.15	37.6 ± 0.2	−8.3 ± 7.2
$SOD1^{I35A}$/holo$SOD1^{dimer}$§	0.53 ± 0.14	35.6 ± 0.4	−4.0 ± 1.8
$SOD1^{I35A}$/BSA§	0.94 ± 0.14	34.6 ± 0.4	−6.1 ± 1.8
$SOD1^{I35A}$/$TTHA^{pwt}$§	1.02 ± 0.13	34.0 ± 0.4	−14.8 ± 3.3
$SOD1^{I35A}$/lysozyme¶	5.72 ± 0.29	21.2 ± 1.0	13.5 ± 2.6

For a complete set of thermodynamic parameters, see Table S2.
*At 37 °C (*SI Materials and Methods*).
†Negative values extrapolated from thermodynamic parameters (*SI Materials and Methods*).
‡Derived from CD data (*SI Controls*).
§Calculated at 100 mg/mL crowder concentration (*SI Controls*).
¶Parameters extrapolated to 100 mg/mL (*SI Controls*).

denatured state. The canonical structures of D, which are observed to be relatively collapsed in pure water (40), seem to expand upon interaction with the intracellular components. Such expansion is also consistent with previous observations of increased unfolding m values in *E. coli* (21) and increased temperature sensitivity of the protein refolding kinetics in mammalian cells (18).

Formal Description of in-Cell Interactions. Provided that the interactions between $SOD1^{I35A}$ and the intracellular environment are overall weak, as is suggested by the NMR data, it is possible to formally describe their effect on the D ⇌ N equilibrium as follows. Assume that one has a number of cellular components {j} of concentration C_j. For each component the interaction potential with $SOD1^{I35A}$ is given by $U_{ij}(\mathbf{r}_{ij},\{\tau\})$, where i denotes either N or D, $\mathbf{r}_{ij}$ is the relative position of i and j, and τ denotes all other coordinates needed to describe the potential. The effect on the D ⇌ N equilibrium of the unspecific interactions $U(\mathbf{r}_{ij})$ can then be quantified using a virial expansion of the osmotic pressure and the second virial coefficient is

$$B_{ij} = -\frac{1}{N(\tau)}\int \exp\left\{\frac{-U_{ij}(\vec{r},\tau)}{kT} - 1\right\} d\tau d\vec{r}, \qquad [3]$$

where $N(\tau)$ is a normalization integral over the variables $\{\tau\}$. The integral over the center of mass separation $d\mathbf{r}_{ij}$ implies that B_{ij} has the dimension of a volume. It follows from the Gibbs–Duhem relation that the chemical potential of $SOD1^{I35A}$ in conformation i is

$$\mu_i = \mu_i^0 + kT \ln C_i + kT \sum_j B_{ij} C_j. \qquad [4]$$

When we neglect higher-order terms in the virial expansion, it follows from Eq. **4** that the in-cell equilibrium constant is

$$K_{D\text{-}N}^{cell} = K_{D\text{-}N}^{ref} \exp\left\{\sum_j (B_{Nj} - B_{Dj}) C_j\right\}, \qquad [5]$$

where $K_{D\text{-}N}^{ref}$ is the in vitro reference. Thus, depending on the difference between the virial coefficients in the cell environment, either N or D can be favored. It is furthermore likely that the sum over cell components j contains both negative and positive terms, where the value of the virial coefficient B_{ij} is determined by the intermolecular potential U_{ij} (Eq. **3**). The main repulsive contribution to the potential U_{ij} is due to the excluded volume interaction. Excluded volume is always present and gives a positive contribution to the virial coefficient, which is larger for the expanded D than for the more compact N. If this was the dominant contribution to B_{ij}, $K_{D\text{-}N}^{cell} < K_{D\text{-}N}^{ref}$ in Eq. **5** and the equilibrium would be shifted toward N: This stabilization of the species of smallest volume is often referred to as the crowding effect (11–13). In addition to the repulsive excluded-volume effect, there are also attractive terms in the intermolecular potentials, giving a negative contribution to the virial coefficient. The dominant, but not the only, attractive contributions stem from local interactions between ionic groups of opposite charge and patchy hydrophobic contacts. For $SOD1^{I35A}$, with a small net charge and closely spaced anionic and cationic groups, the compact N species is expected to show relatively weak local electrostatic interactions with the other cell components. In the more expanded D state, on the other hand, where the charges are spread out and spatially flexible, there are larger possibilities to find such attractive interactions, tending to make $|B_{Dj}| > |B_{Nj}|$ in Eq. **5**. The analogous argument holds for weak hydrophobic interactions where, again, the denatured ensemble will be stabilized due to its higher exposure of spatially amenable hydrophobic patches to the intracellular environment. An illustration of how the expanded D conformation shifts $K_{D\text{-}N}^{cell}$ (Eq. **5**) by providing more opportunities for interactions with cellular components is given by the coupled equilibrium (see Fig. 4).

Clues from in Vitro Crowders. To experimentally delineate the contributions to the in-cell destabilization of $SOD1^{I35A}$, we mapped out the impact of a series of chemically distinct cosolutes in vitro (*SI Data* and Fig. S5 *B–G*). Consistent with predictions from excluded-volume effects (12) (Eqs. **3–5**), the "hard-sphere mimic" ficoll[70] yields a progressive increase of $SOD1^{I35A}$ stability (Fig. 3).

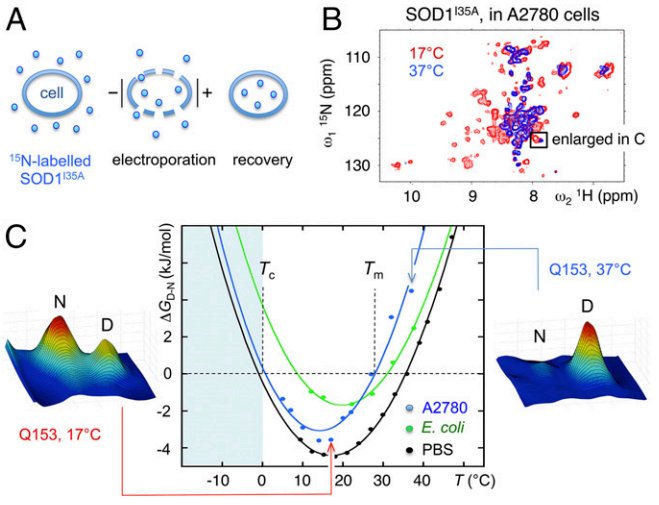

Fig. 2. In-cell quantification of protein stability. (*A*) Schematic illustration of protein delivery by electroporation. The method yields intracellular concentrations of $SOD1^{I35A}$ = 20–30 μM, matching those of human SOD1 in transgenic ALS mice (43) and in vitro aggregation studies (6). (*B*) Two overlaid in-cell HMQC spectra of $SOD1^{I35A}$ showing that the protein is mainly folded at 17 °C (red) and fully unfolded already at 37 °C (blue). An advantage of this detection strategy is that the target protein is retained fully physiological and devoid of potentially interfering spectroscopic reporters. (*C*) $\Delta G_{D\text{-}N}$ vs. temperature profiles based on quantification of the D/N equilibrium from the Q153 cross-peak volumes. The results show that both mammalian and bacterial cells substantially destabilize $SOD1^{I35A}$, albeit in slightly different ways. A common feature is that the in-cell destabilization shifts both cold unfolding (T_C) and melting temperatures (T_m) to the physiological regime (Table 1).

The data show, however, that the origin of this stabilization is molecularly more complex than excluded volume alone, because it is predominantly enthalpic in nature and without notable impact on ΔC_p (Table S2). This is not surprising as osmolytes in general not only occupy volume but also alter the osmotic pressure, yielding multiple components to the effect on protein stability (compare Eq. **3**). Because the ficoll^{70} effect contrasts with the in-cell data, the stabilizing excluded-volume/osmotic pressure contributions seem outweighed by opposing attractive interactions in live cells (Eq. **5**). Next, we benchmarked PEG^{400} that is reported to be an intermediate between a stabilizing osmolyte and a chemical denaturant (41). Similar to ficoll^{70}, PEG^{400} yields an overall stabilization of SOD1^{I35A} (Fig. 3), but with an accompanying increase of ΔC_p (Table S2). The latter indicates expansion of the denatured state of SOD1^{I35A}, consistent with the previously observed PEG^{400} binding (41) and the present in-cell data (Table 1 and Table S2). To better isolate the attractive solute contributions we finally crowded SOD1^{I35A} with a series of different globular proteins. The assumption is that these structurally fixed proteins represent hard spheres with variable surface properties determined by their respective amino acid composition. As a putative "strong" interacting partner we used folded lysozyme with a net positive charge (+8.5 e), allowing multiple electrostatic coordination possibilities with the negatively charged SOD1^{I35A} species (−0.5 e) (Table S3). To minimize any opposing effects of excluded volume, we ran the experiments in the low-concentration regime of [lysozyme] = 0 mg/mL, 30 mg/mL, and 50 mg/mL. In contrast to the inert osmolytes, lysozyme promotes a marked destabilization of SOD1^{I35A} (Fig. 3, Table 1, and Table S2). The net negative bovine serum albumin (BSA) (−8.5 e) and the bacterial putative heavy metal binding protein TTHA^{pwt} (−1.5 e), on the other hand, show no or little effect on SOD1^{I35A} stability, whereas the cysteine-depleted SOD1 dimer, holoSOD1^{dimer} (−5 e), yields a slight stabilization (Fig. 3, Table 1, and Table S2). Taken together, these results show that the effect of surrounding proteins is variable and depends on their detailed surface features. The observation not only complies with the rule that protein–protein interactions are sequence specific, but also emphasizes that the in-cell effect depends on the sequence of the target protein itself: The attraction potential relies on all partners in play (Eq. **3**).

Discussion

In-Cell Modulation of Protein Stability and Conformational Equilibria. The destabilization and unfolding of SOD1^{I35A} in mammalian cells illustrate well how classical in vitro analysis can easily overlook key physiological details (Fig. 2). With the caveat that cultured A2780 cells are not neuronal tissue, the in-cell destabilization observed here would suggest that the aggregation precursor in ALS, i.e., the reduced apoSOD1 monomer with a stability similar to that of SOD1^{I35A}, is largely unfolded in the neurons and not partly structured as envisaged in vitro (29, 42) (*SI Data* and Fig. S5 *J–L*). Such in vivo induced unfolding also explains why soluble apoSOD1 material in spinal cord of ALS mice is fully recognized by antibodies targeting disordered peptide epitopes (43). So, what causes this stability loss? Generally, the steric crowding experienced in the cellular compartment is predicted to stabilize proteins (11, 13). However, proteins engage also in various attractive interactions as they constantly search their environment for functional partners (19, 44–46). If these interactions are on average stronger for the folded state (N), they act stabilizing, and if they are stronger for the unfolded state (D), they act destabilizing (Eqs. **3–5** and Fig. 4). A key distinction here is that, unlike steric crowding, the protein's interactions with the cellular environment depend on sequence identity (19, 45, 46), governed by the same rules as protein folding itself (47). For SOD1^{I35A}, our results suggest that this sequence-specific crosstalk dominates the in-cell experience.

Protein Identity and Cell Environment: Case-Specific Effects. From the perspective of sequence-specific crosstalk (attractive interactions) it is not surprising that experiments targeting different proteins in different cell types and cell lysates yield different results. For example, intracellular stabilization has been observed for the lambda repressor in *E. coli*, using MS hydrogen/deuterium (HD)-exchange analysis (14); for GBI in *E. coli* cytosol (19) and quenched *E. coli* lysate, using NMR HD-exchange analysis (15); and for FRET-labeled Tau (16) and phosphoglycerate kinase (PGK) (17, 18) in mammalian cell lines. The effect on PGK was also seen to vary with cell type, stage of cell cycle, and intracellular localization, underlining the importance of the detailed chemical context surrounding the target protein (17, 25). At the other end of the spectrum, FLASH-labeled CRABP (20) was found to become markedly destabilized in *E. coli* (21), and ubiquitin shows increased HD exchange rates in mammalian cells, suggested to arise from transient interactions with endogenous proteins (22). Similar stability losses are revealed upon titrating of the chymotrypsin inhibitor 2 (CI2) with bacterial lysate (23), by intracellular expression of a mammalian surface antigen (24), and by the mammalian- and bacterial-cell data presented here (Fig. 3, Table 1, and Table S2). Taken together, these observations underline the universal principle of structure–function relationships: The in vivo modulation of protein stability and structural behavior is by no means uniform, but case specific, determined by the interplay between an individual protein and its cellular "encounter interactome."

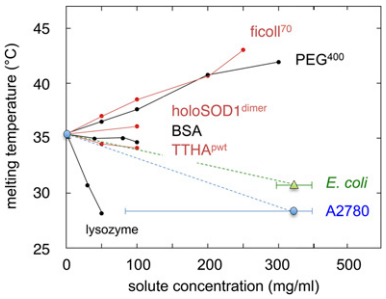

Fig. 3. Comparison of in vivo and in vitro data, showing that osmolytes yield stability changes opposite to those of the cells, whereas protein crowders yield the whole spectrum of effects, underlining the amino acid sequence dependence of the protein solute interactions. The solute concentrations of A2780 and *E. coli* cells show considerable variation in the literature (13), spanning the range of the error bars.

Nature of the Protein–Cell Crosstalk. A ubiquitous source of in-cell interactions is the innate proteostasis system, which "buffers" structural stability and viable protein levels by a complex network of chaperones, transporters, and degradation pathways (8, 48). Somewhat surprisingly, the homogenous and temporally stable two-state equilibrium of SOD1^{I35A} (*SI Controls*) shows that this proteostasis interference is either small or short-lived on the NMR timescale or sequesters strongly a minor, constant, fraction of the protein molecules that blinds out in the analysis and does not take part in the folding equilibrium. There is also no skewing of the $\Delta G_{D\text{-}N}(T)$ profiles (Fig. 2), indicating that the conceivable interference from the proteostasis/chaperone system changes with temperature; i.e., there is no apparent heat- or cold-shock response (48). In terms of thermodynamics, this simplistic behavior allows us to assign the SOD1^{I35A} destabilization to transient interactions alone (23) (Eqs. **3–5** and Fig. 4). The inter-pretation is also in full agreement with the similar effect of homogenous protein solutions (Fig. 3). At present it is not possible to deduce whether our inability to distinguish specific in-cell interactions relates to the specific chaperone-binding affinities of SOD1 itself (49) or reflects a general feature of soluble two-state proteins. Nevertheless, it can be safely assumed that, at a molecular level, one of the primary modulators of weak protein interactions is the side-chain charges, which not only steer macromolecular association and encounter complexes (19, 45) but also maintain solubility by negative design (50–52). The effect

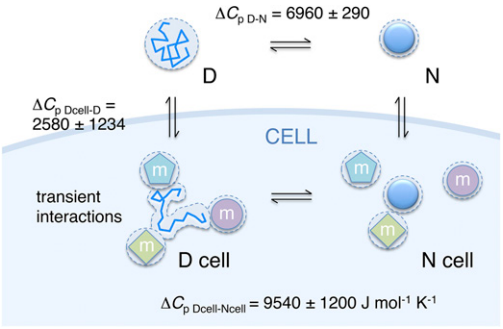

Fig. 4. Coupled folding equilibrium describing the shift toward denatured material upon interaction with the cellular interior, as formalized in Eqs. **3**–**5**. Both the denatured (D) and folded (N) species interact with the cellular molecules (m), but the interactions are stronger/more numerous for the structurally expanded and flexible D species. The increased heat capacity of unfolding (ΔC_p) observed in the cellular compartment (Eqs. **1** and **2** and Fig. 2) is attributed to increased solvent-accessible surface area (dotted boundary) of the denatured ensemble (D cell), promoted by the transient association with neighboring macromolecules (m). Following Elcock's estimate (44), SOD1^{I35A} would at all times experience approximately five putative interaction partners in its immediate cellular environment. Associated thermodynamic parameters are in Table 1 and Table S2.

of lysozyme (+8.5 e) on SOD1^{I35A} (−0.5 e) could then be ascribed to net-charge attraction alone (Table 1). However, there is more to it: The stabilization induced by holoSOD1^{dimer} (−5 e) does not scale with the smaller effects of BSA (−8.5 e) and TTHA^{pwt} (−1.5 e) (Fig. 3). The phenomenon is pinpointed by Sarkar et al. who demonstrated that removal of positively charged proteins from *E. coli* lysates does not significantly reduce CI2 destabilization (53). Like macromolecular interactions in general, each in-cell encounter presents a frustrated (47) conflict between many types of protein interactions, involving also dipoles, hydrophobic contacts, and geometric compatibility. It is easy to envisage that the flexible unfolded chain is here more amenable to find productive contacts than its folded counterpart (Fig. 4).

Quantification. The realization that cells interact with their proteins in a sequence-specific manner allows rational modeling of the in vivo behavior from basic physical–chemical principles. Our results show that mammalian-cell internalization not only reduces SOD1^{I35A} stability but also increases ΔC_p and folding cooperativity: The unfolding transition becomes narrower and more responsive to temperature changes (Fig. 3, Table 1, and Table S2). Following mass action, this indicates that the in-cell environment makes the denatured state more hydrated (39). The same tendencies have previously been hinted at by increased urea *m* values in *E. coli* (21) and by increased temperature dependence of the folding kinetics in mammalian cells (18). In the simplest case, the effect stems from a conformational extension of the unfolded protein itself, perhaps as a result of the flexible chain "spanning" across dispersed interaction sites (13, 54, 55) (Fig. 4). A similar picture is captured by Elcock's full-scale simulation of the bacterial cytoplasm (44) where the stability of individual proteins either decreases or increases, depending on how the unfolded and folded material preferentially interacts with the surrounding. This intrinsic trade-off between steric crowding and weak encounter interactions explains why "passive" osmolytes like ficoll^{70} and PEG^{400} poorly mimic the physiological setting, why different proteins yield different results, and how crowding with chemically distinct proteins can induce the full spectrum of effects (Fig. 3, Table 1, and Table S2). From a theoretical perspective this is reassuring: Protein behavior in vivo seems after all defined by the mixing and environmental tweaking of individual folding funnels (47).

Physiological Occurrence of Cold Unfolding. Intriguingly, the biologically most striking effect of cell internalization is on the cold-unfolding temperature (T_C), which increases to just above zero in mammalian cells and to +8.6 °C in *E. coli* (Table 1). This inherent, yet rarely considered, phenomenon stems from the parabolic temperature dependence of protein stability (56) and moves both the cold-unfolding and melting temperatures of SOD1^{I35A} into the physiological regime (Fig. 3 and Table 1). As analogous behavior is expected for any conformational transition involving sufficient exchange of coordinated water, it is surprising that physiological links to cold unfolding seem missing in the literature, except for an example in Antarctic fish (57). After all, some of the many proteomes of organisms adapted to low temperatures should contain members with structural properties that resemble, or partly overlap with, those of SOD1^{I35A}. Because natural two-state proteins in general are most stable around room temperature (58), the thermal behavior of SOD1^{I35A} is also expected to be representative of marginally stable proteins rather than an odd exception. Regardless of what the physiological occurrence of cold unfolding turns out to be, settling this issue will help delineate the yet poorly understood biological constraints on protein stability.

Concluding Remarks. The answer to how protein behavior in vitro translates to in vivo conditions (13, 44, 59) seems now to be gradually unfolding. Although general confinement and excluded-volume effects must contribute, the rule of the game is in the molecular details: In-cell stability depends not only on the protein sequence itself, but also on how it interacts with its specific intracellular environment. From a sequence perspective alone, different proteins are thus expected to show different in vivo behavior, as is indeed observed in a series of independent in-cell studies, using a broad range of experimental techniques (14–24). Although some of these differences likely stem from experimental and molecular variation other than protein sequence, e.g., intracellular composition, stress response, and physical–chemical variation, they bring attention to the role of organism divergence. Because protein surfaces undergo much more rapid evolution than 3D structures (60), the surfaces exposed by the proteome of bacteria and mammalian cells are not the same. This divergence is found not only in functional interfaces, but also in "background" surfaces outside specific binding epitopes (61), leading to a new balance with the molecules in the cellular medium. The question is then, How will a protein behave in a foreign cellular environment? Our observations show that indeed there is a difference: Above room temperature SOD1^{I35A} is more stable in *E. coli*, whereas at lower temperatures it is better off in the mammalian cells (Fig. 2, Table 1, and Table S2). Along the same line Gruebele and coworkers have found that, even within mammalian cell lines, protein stability depends both on the phase of the cell cycle and on organelle localization (16, 18). Even though the details of these protein–environment relationships are yet to be pinned down, it is clear that the field of physical chemistry has finally moved in vivo (14–24): Molecular phenomena that were previously limited to speculation and inference from in vitro data can now be addressed directly in the environment where proteins are evolved to function.

Materials and Methods

Protein Engineering. Mutagenesis, expression, and purification were as in refs. 26 and 28.

Protein Internalization and in-Cell Analysis. For each in-cell NMR sample, 75–100 × 10^6 cells containing 1 mM ^{15}N isotope-labeled SOD1^{I35A} were electroporated by a Super Electroporator NEPA21 (NePa Gene). Measurements were performed on a Bruker Avance 700 MHz spectrometer. ^{1}H-{^{15}N}-sofast-heteronuclear multiple quantum coherence (62) spectra were used for all in vivo and in vitro experiments. The folded and unfolded populations were determined from the volumes of the C-terminal Q153 cross peaks and $\Delta G_{D\text{-}N}$ was calculated from Eq. **1**.

Structure Determination. Crystals of SOD1^{I35A} were grown at 293 K by the sitting-drop vapor-diffusion method. Data were collected at 100 K on station I911-3 of the MAX IV Laboratory synchrotron, Lund, Sweden. Results have been deposited in the PDB, ID code 4XCR.

ACKNOWLEDGMENTS. We thank Dr. K. Inomata and Dr. H. Tochio for valuable discussions as well as Therese Sörensen and Marchel Stuiver for help with cell sample preparations. Support was from the Swedish Research Council, Swedish Foundation for Strategic Research (MDB1-0030), Hjärnfonden, and The Knut and Alice Wallenberg, Bertil Hållsten, and Magnus Bergwall Foundations. Access to research infrastructure activity in the Seventh Framework Programme of the European Council (Project 261863, Bio-NMR) is acknowledged.

1. Joerger AC, Fersht AR (2008) Structural biology of the tumor suppressor p53. *Annu Rev Biochem* 77:557–582.
2. Bergemalm D, et al. (2006) Overloading of stable and exclusion of unstable human superoxide dismutase-1 variants in mitochondria of murine amyotrophic lateral sclerosis models. *J Neurosci* 26(16):4147–4154.
3. Luchinat E, et al. (2014) In-cell NMR reveals potential precursor of toxic species from SOD1 fALS mutants. *Nat Commun* 5:5502.
4. Byström R, Andersen PM, Gröbner G, Oliveberg M (2010) SOD1 mutations targeting surface hydrogen bonds promote amyotrophic lateral sclerosis without reducing apostate stability. *J Biol Chem* 285(25):19544–19552.
5. Ciryam P, Tartaglia GG, Morimoto RI, Dobson CM, Vendruscolo M (2013) Widespread aggregation and neurodegenerative diseases are associated with supersaturated proteins. *Cell Reports* 5(3):781–790.
6. Lang L, Kurnik M, Danielsson J, Oliveberg M (2012) Fibrillation precursor of superoxide dismutase 1 revealed by gradual tuning of the protein-folding equilibrium. *Proc Natl Acad Sci USA* 109(44):17868–17873.
7. Eichner T, Kalverda AP, Thompson GS, Homans SW, Radford SE (2011) Conformational conversion during amyloid formation at atomic resolution. *Mol Cell* 41(2):161–172.
8. Balch WE, Morimoto RI, Dillin A, Kelly JW (2008) Adapting proteostasis for disease intervention. *Science* 319(5865):916–919.
9. Beckman JS, Carson M, Smith CD, Koppenol WH (1993) ALS, SOD and peroxynitrite. *Nature* 364(6438):584.
10. Hipp MS, Park SH, Hartl FU (2014) Proteostasis impairment in protein-misfolding and -aggregation diseases. *Trends Cell Biol* 24(9):506–514.
11. Zhou HX, Rivas G, Minton AP (2008) Macromolecular crowding and confinement: biochemical, biophysical, and potential physiological consequences. *Annu Rev Biophys* 37: 375–397.
12. Cheung MS, Klimov D, Thirumalai D (2005) Molecular crowding enhances native state stability and refolding rates of globular proteins. *Proc Natl Acad Sci USA* 102(13): 4753–4758.
13. Ellis RJ, Minton AP (2003) Cell biology: Join the crowd. *Nature* 425(6953):27–28.
14. Ghaemmaghami S, Oas TG (2001) Quantitative protein stability measurement in vivo. *Nat Struct Biol* 8(10):879–882.
15. Monteith WB, Pielak GJ (2014) Residue level quantification of protein stability in living cells. *Proc Natl Acad Sci USA* 111(31):11335–11340.
16. Dhar A, Ebbinghaus S, Shen Z, Mishra T, Gruebele M (2010) The diffusion coefficient for PGK folding in eukaryotic cells. *Biophys J* 99(9):L69–L71.
17. Dhar A, et al. (2011) Protein stability and folding kinetics in the nucleus and endoplasmic reticulum of eucaryotic cells. *Biophys J* 101(2):421–430.
18. Guo M, Xu Y, Gruebele M (2012) Temperature dependence of protein folding kinetics in living cells. *Proc Natl Acad Sci USA* 109(44):17863–17867.
19. Monteith WB, Cohen RD, Smith AE, Guzman-Cisneros E, Pielak GJ (2015) Quinary structure modulates protein stability in cells. *Proc Natl Acad Sci USA* 112(6):1739–1742.
20. Ignatova Z, et al. (2007) From the test tube to the cell: Exploring the folding and aggregation of a beta-clam protein. *Biopolymers* 88(2):157–163.
21. Ignatova Z, Gierasch LM (2007) Effects of osmolytes on protein folding and aggregation in cells. *Methods Enzymol* 428:355–372.
22. Inomata K, et al. (2009) High-resolution multi-dimensional NMR spectroscopy of proteins in human cells. *Nature* 458(7234):106–109.
23. Sarkar M, Smith AE, Pielak GJ (2013) Impact of reconstituted cytosol on protein stability. *Proc Natl Acad Sci USA* 110(48):19342–19347.
24. Guzman I, Gelman H, Tai J, Gruebele M (2014) The extracellular protein VlsE is destabilized inside cells. *J Mol Biol* 426(1):11–20.
25. Wirth AJ, Platkov M, Gruebele M (2013) Temporal variation of a protein folding energy landscape in the cell. *J Am Chem Soc* 135(51):19215–19221.
26. Danielsson J, Kurnik M, Lang L, Oliveberg M (2011) Cutting off functional loops from homodimeric enzyme superoxide dismutase 1 (SOD1) leaves monomeric β-barrels. *J Biol Chem* 286(38):33070–33083.
27. Leinartaite L, Saraboji K, Nordlund A, Logan DT, Oliveberg M (2010) Folding catalysis by transient coordination of Zn2+ to the Cu ligands of the ALS-associated enzyme Cu/Zn superoxide dismutase 1. *J Am Chem Soc* 132(38):13495–13504.
28. Lindberg MJ, Normark J, Holmgren A, Oliveberg M (2004) Folding of human superoxide dismutase: Disulfide reduction prevents dimerization and produces marginally stable monomers. *Proc Natl Acad Sci USA* 101(45):15893–15898.
29. Nordlund A, Oliveberg M (2006) Folding of Cu/Zn superoxide dismutase suggests structural hotspots for gain of neurotoxic function in ALS: Parallels to precursors in amyloid disease. *Proc Natl Acad Sci USA* 103(27):10218–10223.
30. Nordlund A, et al. (2009) Functional features cause misfolding of the ALS-provoking enzyme SOD1. *Proc Natl Acad Sci USA* 106(24):9667–9672.
31. Danielsson J, et al. (2013) Global structural motions from the strain of a single hydrogen bond. *Proc Natl Acad Sci USA* 110(10):3829–3834.
32. Danielsson J, et al. (2013) Pruning the ALS-associated protein SOD1 for in-cell NMR. *J Am Chem Soc* 135(28):10266–10269.
33. Hamilton TC, Young RC, Ozols RF (1984) Experimental model systems of ovarian cancer: Applications to the design and evaluation of new treatment approaches. *Semin Oncol* 11(3):285–298.
34. Bergh J, et al. (2015) Structural and kinetic analysis of protein-aggregate strains in vivo using binary epitope mapping. *Proc Natl Acad Sci USA* 112(14):4489–4494.
35. Lang L, et al. (2015) SOD1 aggregation in ALS mice shows simplistic test tube behavior. *Proc Natl Acad Sci USA* 112(32):9878–9883.
36. Westman NG, Marklund SL (1981) Copper- and zinc-containing superoxide dismutase and manganese-containing superoxide dismutase in human tissues and human malignant tumors. *Cancer Res* 41(7):2962–2966.
37. Tanford C (1968) Protein denaturation. *Adv Protein Chem* 23:121–282.
38. Oliveberg M, Tan YJ, Fersht AR (1995) Negative activation enthalpies in the kinetics of protein folding. *Proc Natl Acad Sci USA* 92(19):8926–8929.
39. Myers JK, Pace CN, Scholtz JM (1995) Denaturant m values and heat capacity changes: relation to changes in accessible surface areas of protein unfolding. *Protein Sci* 4(10): 2138–2148.
40. Wuttke R, et al. (2014) Temperature-dependent solvation modulates the dimensions of disordered proteins. *Proc Natl Acad Sci USA* 111(14):5213–5218.
41. Senske M, et al. (2014) Protein stabilization by macromolecular crowding through enthalpy rather than entropy. *J Am Chem Soc* 136(25):9036–9041.
42. Chattopadhyay M, et al. (2008) Initiation and elongation in fibrillation of ALS-linked superoxide dismutase. *Proc Natl Acad Sci USA* 105(48):18663–18668.
43. Zetterström P, et al. (2007) Soluble misfolded subfractions of mutant superoxide dismutase-1s are enriched in spinal cords throughout life in murine ALS models. *Proc Natl Acad Sci USA* 104(35):14157–14162.
44. McGuffee SR, Elcock AH (2010) Diffusion, crowding & protein stability in a dynamic molecular model of the bacterial cytoplasm. *PLoS Comput Biol* 6(3):e1000694.
45. Schreiber G, Fersht AR (1996) Rapid, electrostatically assisted association of proteins. *Nat Struct Biol* 3(5):427–431.
46. Sugase K, Dyson HJ, Wright PE (2007) Mechanism of coupled folding and binding of an intrinsically disordered protein. *Nature* 447(7147):1021–1025.
47. Oliveberg M, Wolynes PG (2005) The experimental survey of protein-folding energy landscapes. *Q Rev Biophys* 38(3):245–288.
48. Lindquist SL, Kelly JW (2011) Chemical and biological approaches for adapting proteostasis to ameliorate protein misfolding and aggregation diseases: Progress and prognosis. *Cold Spring Harb Perspect Biol* 3(12):a004507.
49. Wang J, et al. (2009) Progressive aggregation despite chaperone associations of a mutant SOD1-YFP in transgenic mice that develop ALS. *Proc Natl Acad Sci USA* 106(5): 1392–1397.
50. Otzen DE, Kristensen O, Oliveberg M (2000) Designed protein tetramer zipped together with a hydrophobic Alzheimer homology: A structural clue to amyloid assembly. *Proc Natl Acad Sci USA* 97(18):9907–9912.
51. Vendruscolo M, Dobson CM (2007) Chemical biology: More charges against aggregation. *Nature* 449(7162):555.
52. Kurnik M, Hedberg L, Danielsson J, Oliveberg M (2012) Folding without charges. *Proc Natl Acad Sci USA* 109(15):5705–5710.
53. Sarkar M, Lu J, Pielak GJ (2014) Protein crowder charge and protein stability. *Biochemistry* 53(10):1601–1606.
54. Vuzman D, Levy Y (2010) DNA search efficiency is modulated by charge composition and distribution in the intrinsically disordered tail. *Proc Natl Acad Sci USA* 107(49): 21004–21009.
55. Kudlay A, Cheung MS, Thirumalai D (2012) Influence of the shape of crowding particles on the structural transitions in a polymer. *J Phys Chem B* 116(29):8513–8522.
56. Privalov PL, Makhatadze GI (1993) Contribution of hydration to protein folding thermodynamics. II. The entropy and Gibbs energy of hydration. *J Mol Biol* 232(2):660–679.
57. Todgham AE, Hoaglund EA, Hofmann GE (2007) Is cold the new hot? Elevated ubiquitin-conjugated protein levels in tissues of Antarctic fish as evidence for cold-denaturation of proteins in vivo. *J Comp Physiol B* 177(8):857–866.
58. Kumar S, Tsai CJ, Nussinov R (2002) Maximal stabilities of reversible two-state proteins. *Biochemistry* 41(17):5359–5374.
59. Frembgen-Kesner T, Elcock AH (2013) Computer simulations of the bacterial cytoplasm. *Biophys Rev* 5(2):109–119.
60. Gerstein M, Sonnhammer EL, Chothia C (1994) Volume changes in protein evolution. *J Mol Biol* 236(4):1067–1078.
61. Göbel U, Sander C, Schneider R, Valencia A (1994) Correlated mutations and residue contacts in proteins. *Proteins* 18(4):309–317.
62. Schanda P, Brutscher B (2005) Very fast two-dimensional NMR spectroscopy for real-time investigation of dynamic events in proteins on the time scale of seconds. *J Am Chem Soc* 127(22):8014–8015.
63. Becktel WJ, Schellman JA (1987) Protein stability curves. *Biopolymers* 26(11):1859–1877.
64. Collaborative Computational Project, Number 4 (1994) The CCP4 suite: Programs for protein crystallography. *Acta Crystallogr D Biol Crystallogr* 50(Pt 5):760–763.
65. Emsley P, Cowtan K (2004) Coot: Model-building tools for molecular graphics. *Acta Crystallogr D Biol Crystallogr* 60(Pt 12 Pt 1):2126–2132.
66. Dalby PA, Oliveberg M, Fersht AR (1998) Folding intermediates of wild-type and mutants of barnase. I. Use of phi-value analysis and m-values to probe the cooperative nature of the folding pre-equilibrium. *J Mol Biol* 276(3):625–646.

Supporting Information

Danielsson et al. 10.1073/pnas.1511308112

SI Materials and Methods

Mutagenesis, Expression, and Purification. Mutagenesis, expression, and purification of $SOD1^{barrel}$, $SOD1^{I35A}$, $SOD1^{I35A/G93A}$, $SOD1^{C6A/F50E/G51E/C111A}$ ($SOD1^{pwt}$), and $SOD1^{C6A/C111A}$ ($holoSOD1^{dimer}$) were as in refs. 26 and 28. The gene encoding TTHA1718, subcloned into the vector pET3a were purchased from GenScript. The double mutation C11S/C14S ($TTHA^{pwt}$) was introduced by the site-directed mutagenesis kit (Agilent Technologies) to disrupt metal binding, resulting in a pseudo-wild-type variant, $TTHA^{pwt}$. The protein was expressed in *Escherichia coli* BL21(DE3) (Invitrogen). Cells were grown in 2× LB medium at 37 °C in the presence of 100 μg/mL carbenicillin and expression was induced with 0.5 mM isopropyl 1-thio-β-D-galactopyranoside at OD = 0.7–0.9. Overexpression was overnight at 23 °C. Cells were harvested [6,200 × *g*, 15 min, 4 °C in a JLA 8.1000 rotor (Beckman)] and the pellet was resuspended in 10 mM Tris·HCl at pH 7.5. Cells were then lysed by sonication and centrifuged [39,000 × *g*, 30 min, 4 °C in a JA 25.50 rotor (Beckman)] and the supernatant was treated at 70 °C for 10 min. After another centrifugation step [39,000 × *g*, 30 min, 4 °C in a JA 25.50 rotor (Beckman)], the supernatant was loaded to a Q-Sepharose anion exchange column (GE Healthcare), and the protein was eluted by a linear 0–35% 1 M NaCl gradient in 10 mM Tris·HCl at pH 7.5. The fractions containing $TTHA^{pwt}$ were loaded to a Sephacryl S-100 High Resolution gel filtration column (GE Healthcare) and eluted with 500 mM NaCl, 10 mM Tris·HCl at pH 7.5. Purity was analyzed in each step by SDS/PAGE (Bio-Rad). The pure protein was finally desalted by dialysis in pure milliQ H_2O and concentrated for in vitro crowding studies.

Sample Preparation for in Vitro Crowding Studies. Bovine serum albumin (BSA), chicken egg white lysozyme, and Ficoll 70 were purchased from Sigma, and PEG^{400} was purchased from KEBO. $TTHA^{pwt}$ and $holoSOD1^{dimer}$ were produced as described above. Purchased proteins were dissolved and dialyzed in milliQ H_2O to remove any buffer salts, followed by concentration for NMR sample preparation. In vitro crowding experiments were performed in 20 mM phosphate buffer at pH 6.5 + 150 mM NaCl (PBS) or in phosphate buffer at pH 7 (PB) with 10% D_2O and 0.4 mM $SOD1^{I35A}$ and different amounts of crowding agents.

NMR Temperature Scan Analysis. NMR temperature scan data were used to determine the population of folded (N) and unfolded (D) protein as a function of temperature, and from these populations $\Delta G_{D\text{-}N}$ was calculated according to Eq. **1** in the main text. The temperature dependence of $\Delta G_{D\text{-}N}$ was fitted to (63)

$$\Delta G_{D\text{-}N}(T) = \Delta H_{D\text{-}N}(T_0) - T\Delta S_{D\text{-}N}(T_0) + \Delta C_p\left[T - T_0 - T\ln\left(\frac{T}{T_0}\right)\right], \quad \text{[S1]}$$

where T_0 is the reference temperature, and $\Delta H_{D\text{-}N}(T_0)$ and $\Delta S_{D\text{-}N}(T_0)$ are the entropy and enthalpy at T_0. Data were analyzed using KaleidaGraph (Synergy Software).

Sample Preparation for in Vitro pH Titration Studies. Each NMR sample contained 0.4 mM $SOD1^{I35A}$, 20 mM phosphate buffer (at a pH range between 5.8 and 7.6), 150 mM NaCl, 10% (vol/vol) D_2O, and 50 μM DSS. The final pH of each sample was determined with a pH electrode. The pH titration experiments were performed at 17 °C where $SOD1^{I35A}$ has a maximum stability.

Sample Preparation for in-*E. coli* Stability Studies. BL21(DE3)pLysS cells (Invitrogen), carrying the pET3a-$SOD1^{I35A}$ plasmid, were grown overnight at 37 °C in 400 mL of unlabeled 2× LB medium in the presence of 100 μg/mL carbenicillin and 34 μg/mL chloramphenicol, harvested (800 × *g*, 8 min at 4 °C), and resuspended in 200 mL M9 medium containing 1 g/L $^{15}NH_4Cl$ and 2 g/L glucose. ^{15}N-labeled $SOD1^{I35A}$ was overexpressed 5 h at 37 °C after induction by 1-thio-β-D-galactopyranoside (final concentration 0.5 mM). Cells were harvested (800 × *g*, 8 min at 4 °C) and the pellet was gently resuspended to 1 g/mL in M9 buffer containing 10% (vol/vol) D_2O. After each NMR measurement, the cells were pelleted by centrifugation and the supernatant was checked for protein leakage. The pellet was finally resuspended in M9 and 10% D_2O for lysate control experiments.

Folding Kinetics. The urea used for protein denaturation was ultrapure (MP Biomedicals). Kinetic measurements were on a PIStar-180 stopped-flow apparatus (Applied Photophysics) with excitation at 280 nm and emission collected with a 320-nm long-pass filter. Reduction of $SOD1^{pwt}$ was by addition of 1 mM Tris (2-carboxyethyl) phosphine (TCEP) and incubation for 2 h at 37 °C. All kinetic measurements were performed in 20 mM phosphate buffer at pH 7 or 6.5, with or without 150 mM NaCl, and a final protein concentration of 4 μM. The observed folding kinetics were fitted to (28)

$$\log k_{obs} = \log\left(k_f + k_u\right) = \log\left(10^{\log k_f^{H_2O} + m_f[\text{urea}]} + 10^{\log k_u^{H_2O} + m_u[\text{urea}]}\right), \quad \text{[S2]}$$

where k_{obs} is the observed rate constant, k_f and k_u are the refolding and unfolding rate constants, respectively, and $\log k_f^{H_2O}$ and $\log k_u^{H_2O}$ are the folding and unfolding rate constants extrapolated to [urea] = 0 M. m_f and m_u are given by the slopes of the linear fit, describing the change in solvent exposure going from D to the transition state (TS) and from N to TS, respectively (28). Data analysis was with KaleidaGraph (Synergy Software).

Circular Dichroism Spectroscopy. CD spectra were recorded using a JASCO-815 CD spectrometer with a Peltier temperature control system. Temperature scans from 5 °C to 65–95 °C were recorded by integrating the signal between 222 nm and 234 nm. The protein concentration was 2 μM in 10 mM phosphate buffer, with pH ranging from 5.8 to 7.6. The CD scans were fitted to

$$\Theta_{obs} = \frac{\Theta_N e^{\left(\Delta H(T/T_m - 1)/RT\right)}}{1 + e^{\Delta H(T/T_m - 1)/RT}} + \Theta_D, \quad \text{[S3]}$$

where Θ_{obs} is the mean observed ellipticity at 220–230 nm, and Θ_N and Θ_D are the ellipticities of N and D, respectively. Data analysis was with Igor Pro.

Crystallization, Data Collection, and Structural Determination. Crystals of $SOD1^{I35A}$ were grown at 293 K by the sitting-drop vapor-diffusion method. A total of 50 nL protein solution (11.5 mg mL^{-1} in 10 mM Tris, pH 7.5) was mixed with 150 nL reservoir solution containing 0.1 M Bis·Tris at pH 5.5 and 2.0 M ammonium sulfate. The crystals grew to maximum dimensions of 50 × 50 × 20 μm in 2 mo. The crystals were soaked in mother liquor containing 15% glycerol before flash-freezing in a cold nitrogen stream at 100 K. Data were collected at 100 K on station I911-3 of the MAX IV Laboratory synchrotron, Lund, Sweden; processed with iMosflm;

and merged using Aimless from the CCP4 suite (64). The crystal diffracted weakly, giving data to 3.6 Å resolution. The structure was solved by molecular replacement with Molrep (64), using the $SOD1^{barrel}$ (26, 31) (PDB code 4BCZ) as the initial search model. Model building and refinement were carried out using Coot (65), Phoenix, and Refmac5 (64), and the structure was analyzed with Procheck (64). Data and model quality statistics are presented in Table S1. The final coordinates and structure factors have been deposited in the Protein Data Bank with code 4XCR. Figures of $SOD1^{I35A}$ were prepared with PyMOL.

NMR Spectroscopy. Measurements were performed on a Bruker Avance 700-MHz or 500-MHz spectrometer with a triple-resonance cryoprobe. ^{1}H-{^{15}N}-sofast-heteronuclear multiple quantum coherence (HMQC) (62) spectra were used for all thermal stability experiments, in vitro crowding experiments, and in vitro pH titration experiments, with 32 scans per increment and an interscan delay of 0.2 s for a total duration of about 18 min. Temperature scan experiments were acquired at 278–320 K, in steps of 3–5 K with 5 min equilibrium time between each measurement to ensure temperature stability. The folded and unfolded populations were determined from the volumes of the C-terminal Q153 cross peaks at (8.129, 125.2) ppm and (8.038, 125.6) ppm. For the in-*E. coli* stability experiments, we used one sample for each temperature.

In-Cell NMR Sample Preparation. A2780 cells (Sigma Aldrich) were grown at 37 °C and 5% CO_2 in TC culture dishes with RPMI media (Life technologies), containing 10% (vol/vol) FBS (Life Technologies), until >80% confluence was reached. For each in-cell NMR sample, 75–100 × 10^6 cells were harvested by Trypsin/EDTA (Life Technologies) treatment and resuspended in Opti-MEM media (Life Technologies), containing 1 mM ^{15}N isotope-labeled $SOD1^{I35A}$, to adjust the final density to 30 × 10^6 cells/mL. Cell suspensions were aliquoted into 100-μL fractions in electroporation cuvettes and electroporated by a Super Electroporator NEPA21 (NePa Gene) with a single 110-V, 14-ms, poration pulse followed by five 20-V, 50-ms, transfer pulses with a 50-ms delay in between. The total energy transferred was 3.5–4.0 J. Cells were then transferred to TC culture dishes and placed in the incubator for 4 h of recovery. Subsequently, dead cells were washed away and the surviving cells were collected by Trypsin/EDTA treatment and resuspended in Opti-MEM media (Life Technologies), supplemented with 10% D_2O. The survival was 25–88%, with an average of 60%. Finally, the cells were gently transferred to the NMR tube for data acquisition. After each NMR experiment, the cells were gently centrifuged and the supernatant was checked for protein leakage.

SI Controls

Control of Internalization. A prerequisite for in-cell NMR is that the NMR signal stems from isotope-labeled protein inside the cells. In the sample preparation the cells were washed carefully two times after the recovery period, to remove any proteins outside the cells. This minimizes the risk for signal from proteins in the solute. Even so, after packing and during experiment, the cells are subject to stress and protein may leak out or the cells may die and lyse, resulting in an accumulation of isotope-labeled protein outside the cells. Thus, to ensure that the signals used in this study stem from internalized protein only, we measured a 1D ^{1}H-{^{15}N}-HMQC spectrum directly after the 2D acquisition. After this experiment the cells were collected and gently centrifuged and a 1D ^{1}H-{^{15}N}-HMQC spectrum on the supernatant with the same setup was recorded. A leakage <10% is assumed to be insignificant for the NMR signal. All leakage spectra are shown in Fig. S2*A*.

In-Cell NMR Spectrum of $SOD1^{barrel}$. The fully folded $SOD1^{barrel}$ protein displays a well-resolved, high-quality in-cell HMQC spectrum after internalization by electroporation (Fig. S2*B*).

Determination of in-Cell pH. To be able to adjust all in vitro controls to the in-cell pH, we used in-cell NMR to determine the cytosolic pH. The readout was pH-sensitive chemical shifts of $SOD1^{I35A}$, especially manifested by protonation of the histidine side chains within the physiological pH range, following the same protocol as previously described (32). In short, we determined the in vitro chemical shifts at pH 6.0–8.0 in steps of 0.2 units. By direct comparison of the four most affected cross peaks we estimated the cytosolic pH to 6.5 ± 0.1 (Fig. S2*C*).

Structural Properties of $SOD1^{I35A}$. To ensure that the folded structure of the marginally stable $SOD1^{I35A}$ is similar to that of the wild-type $SOD1^{barrel}$, the crystal structure of $SOD1^{I35A}$ was determined. Data collection and structure refinement statistics are summarized in Table S1. Despite extensive crystal optimization, the marginally stable $SOD1^{I35A}$ do not yield crystals giving data allowing resolution below 3.6 Å. Nevertheless, data show that $SOD1^{I35A}$ and $SOD1^{barrel}$ have very similar overall backbone structures (Fig. S3*A*), with a rms deviation between superimposed C^{α} atoms of 0.36 Å for chain A and 0.38 Å for chain B, respectively. The structures, however, differ in temperature factors (Fig. S3 *B* and *C*), where the average B factor of $SOD1^{I35A}$ (68.5 $Å^2$) is higher than that of $SOD1^{barrel}$ (36.6 $Å^2$). This apparent difference in structural flexibility is consistent with the low-resolution diffraction of $SOD1^{I35A}$ crystals (3.6 Å), compared with $SOD1^{barrel}$ (1.93 Å), despite the two proteins having the same space group and quite similar unit cell dimensions.

The wild-type-like structure of $SOD1^{I35A}$ is also manifested by the close resemblance of the $SOD1^{I35A}$ and $SOD1^{barrel}$ ^{1}H-{^{15}N}-HSQC NMR spectra (Fig. S3 *D* and *E*). Moreover, both proteins exhibit clear two-state folding transition, with similar m_u values of 0.3 for SOD^{barrel} (26) and 0.35 for $SOD1^{I35A}$ (Fig. S3*F*). Taken together, the crystallographic, NMR, and folding data suggest that the SOD1 structure is overall unaffected by the core mutation I35A. Finally, we calculated the surface charge distribution for $SOD1^{barrel}$ and $SOD1^{I35A}$, using the build-in PyMol module. We find no changes in electrostatic surface properties upon mutation of I35A (Fig. S3 *D* and *E*).

Temperature- and Viscosity-Induced NMR Relaxation Effects. The accuracy of the population determination is directly linked to the accuracy in peak volume determination that, in turn, is dependent on the signal-to-noise ratio. Upon determining the peak volume, the signal was summed over a box of an area well covering the cross peak. Significant line broadening could still introduce a systematic error in the population determination. The relaxation properties, and thus the line widths, of the cross peaks corresponding to the folded and unfolded states are expected to be different, where the longer effective correlation time of the folded state results in faster relaxation and wider cross peaks. If the line-broadening effect is different between cross peaks corresponding to the folded ($P_{N,Q153}$) and unfolded states ($P_{D,Q153}$), this could then bias the determined free energy landscape. To minimize these effects we used the C-terminal Q153 as a probe, as this is highly flexible also in the folded state (26). Furthermore, the C-terminal NH is in slow exchange with water protons at all studied temperatures and pHs, ensuring minimum involvement from exchange effects.

To understand the effect of line broadening on the population determination, we performed NMR-spectra simulation where we generated cross peaks with varying line width and used a sum-over-a-box population determination. Indeed, assuming the temperature dependence for the folded population as determined in vitro, the free energy profile determined in cells could be reproduced by

just introducing a significantly stronger line-broadening effect on $P_{N,Q153}$ (Fig. S3*G*). However, to achieve this effect the line width of $P_{N,Q153}$ needs to be more than a factor of 10 larger than for $P_{D,Q153}$, which is far above the determined and expected difference. In addition, the temperature dependence needs to have a parabolic shape (Fig. S3*H*), and that is not physically reasonable. Furthermore, direct measurement of the line widths in the in-cell NMR spectra shows only small temperature dependence of the overall small line widths difference between $P_{N,Q153}$ and $P_{D,Q153}$ (Fig. S3*H*).

To study the effect on viscosity and temperature changes we recorded a temperature series for the folded $SOD1^{barrel}$ in 20% glycerol as well as the unfolded $SOD1^{barrel}$ in 8 M urea, corresponding to the same viscosity. Reassuringly, we found that the systematic errors monotonically decrease with temperature, and at all temperatures >270 K the uncertainty in population determination corresponds to $\Delta G_{D\text{-}N} < 250$ J·mol^{-1} (Fig. S3*I*).

The cross-peak line width is directly linked to the NMR relaxation rate R_2 and, to estimate the effect on local mobility and thereby relaxation by temperature, we determined R_2 for $P_{N,Q153}$ and $P_{D,Q153}$ of $SOD1^{I35A}$ at three temperatures (Fig. S3*J*). As expected the R_2 difference between the folded and unfolded states decreases with temperature, whereas the ratio $R_{2,D}/R_{2,N}$ is relatively constant in this temperature interval. Changing the temperature from 7 °C to 37 °C reduces this ratio from 4.2 to 3.2, corresponding to a change in line width of less than a factor of 2.

Finally, to test the temperature dependence of $P_{N,Q153}$ and $P_{D,Q153}$ simultaneously with populations of D and N that do not change with temperature, we constructed a protein variant, $SOD1^{I35A/G93A}$, destabilized to such a degree that it never folds under physiological conditions, mimicking $P_{D,Q153}$. $SOD1^{I35A/G93A}$ was mixed in equal concentrations with $SOD1^{barrel}$, mimicking $P_{N,Q153}$ (Fig. S3*K*). In the temperature interval studied here (4–40 °C) $SOD1^{barrel}$ is fully folded and $SOD1^{I35A/G93A}$ is completely unfolded, which means that the relative population of unfolded and folded material in the mixture will be constant under change of temperature. Direct determination of the peak volumes shows temperature dependence for both the folded and the unfolded Q153. However, the temperature dependence is similar for both the peaks; i.e., the population determined from these peak volumes is constant, $p_U = p_F = 0.5$ (Fig. S3*L*).

Comparison of CD and NMR Data. As an independent control that the thermodynamic parameters extracted from population determinations by NMR are valid, we performed CD-detected thermal melting experiments. From these direct CD melt curves, ΔC_p was determined to 6.3 ± 0.8 kJ·mol^{-1}, in good agreement with NMR-derived values. In addition we used CD to determine T_m and ΔH of $SOD1^{I35A}$ at different pH values to obtain yet another measure of ΔC_p, from the relationship $\Delta CP = \delta\Delta H/\delta T_m$ (63) (Fig. S4 *A* and *B*). Again we found excellent agreement between the NMR-derived $\Delta C_p = 7.0 \pm 0.4$ kJ·mol^{-1}·K^{-1} and $\Delta CP = \delta\Delta H/\delta T_m = 7.1 \pm 0.9$ kJ·mol^{-1}·K^{-1}.

Sample Stability. To ensure that all samples were stable during the course of the experiment, we recorded a 1D ^{1}H-{^{15}N}-HMQC before and after the 2D experiment used for population determination. For all temperatures, the samples were found to be stable over 4 h (Fig. S4*C*). At higher temperatures, $T > 300$ K, a slight shift in populations was sometimes indicated. To check whether this shift is significant, we recorded two 2D HMQCs at 310 K and determined the population for each experiment. No significant difference was found, showing that the population drift is small and does not affect the overall results.

pH and Ionic-Strength Effects. As the $SOD1^{I35A}$ is a marginally stable protein, a small change in sample conditions can result in large population shifts. Thus, to ensure that the in-cell destabilization is not a pure pH and/or ionic strength effect we performed a series of controls as follows. First, we determined by NMR the folded population of $SOD1^{I35A}$ at 310 K, at pH values ranging from 5.8 to 7.6, and found negligible differences (Fig. S4*D*). The effect on the thermodynamics by altering the pH was then further studied by determination of the melting temperature at varying pH, and here we found significant effects outside the interval pH 6–7; within this interval the melting temperatures are rather unaffected, consistent with NMR data (Fig. S4*E*). To visualize, qualitatively, the worst-case effect on the $\Delta G_{D\text{-}N}$ vs. temperature profile, the pH dependence of the thermodynamic parameters was included and two extreme $\Delta G_{D\text{-}N}$ profiles were calculated (Fig. S4*F*).

$SOD1^{I35A}$ is slightly destabilized by salt up to physiological concentrations, and the change is monotonic and decreases the melting temperature by ∼5 °C (Fig. S4 *G* and *H*). To mimic the in-cell conditions as well as possible we performed all in vitro controls in 150 mM NaCl.

SI Data

Mapping out the Effects of Various in Vitro Crowders. All $SOD1^{I35A}$ $\Delta G_{D\text{-}N}$ profiles used to determine the temperature dependence of the thermodynamic parameters in various solutes are shown in Fig. S4 *A*–*G*. Fig. S4*A* shows the results from thermal scans in *E. coli* lysate, displaying a marked dependence of sample preparation conditions. Because of the poor reproducibility of these experiments, we chose not to include lysate data in the analysis, but only the results from intact *E. coli* cells (Fig. 3, main text). The cross peaks of the in-*E. coli* spectra are more line broadened than in mammalian cells, but the C-terminal Q153 cross peaks are still adequate for reliable determination of the D and N populations of $SOD1^{I35A}$ (Fig. S4 *H* and *I*).

Similarity Between $SOD1^{I35A}$ and Monomeric Reduced Full-Length $apoSOD1^{pwt}$. The monomeric variant $apoSOD1^{pwt}$ ($SOD1^{C6A/C111A/F50E/G51E}$) has been extensively used as a model for the aggregation precursor of ALS (28). In its reduced form, $apoSOD1^{pwt}$ has structural properties very similar to those of $SOD1^{I35A}$, with respect to thermal melting temperature, the temperature dependence of the thermodynamic parameters in Eq. **2** (main text), and unfolding rates (Fig. S5 *J*–*L*). Due to the low midpoint of reduced $SOD1^{pwt}$ (very close to 0 M urea), the refolding rates could not be determined directly from chevron plots at 37 °C.

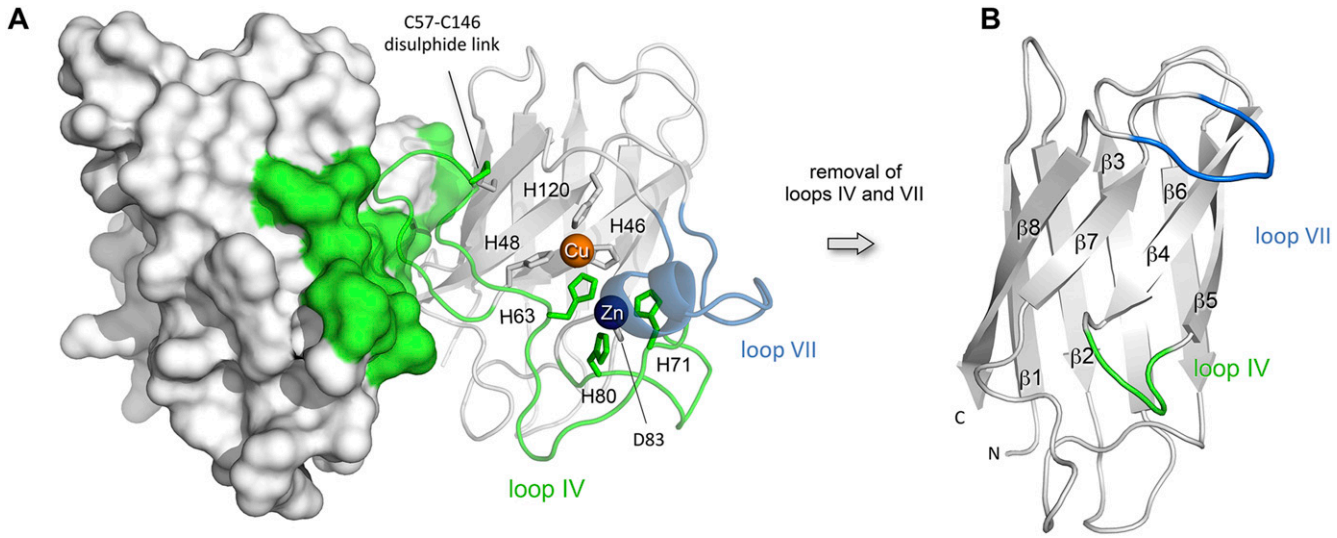

Fig. S1. The structure of the native SOD1 dimer (PDB code 1HL5) and the loop regions removed by protein engineering. (*A*) In the native SOD1 dimer the long loops IV and VII adapt a compact and highly ordered structure around the active site, where loop IV also forms part of the dimer interface (green). The left-hand monomer is shown as accessible surface (1.4 Å probe radius) whereas the right-hand monomer is represented as a cartoon. Highlighted are the residues coordinating the active-site $Cu^{1+/2+}$ and Zn^{2+} ions and the C57–C146 disulfide linkage between loop IV and the central β-barrel. (*B*) Removal of loops IV and VII from apoSOD1 reduces the dimer interface as well as the metal binding moieties and leads to soluble apoSOD1^{barrel} monomers (PDB code 4BCZ). The truncated loops IV and VII are highlighted in green and blue, respectively. (Adapted from ref. 26.)

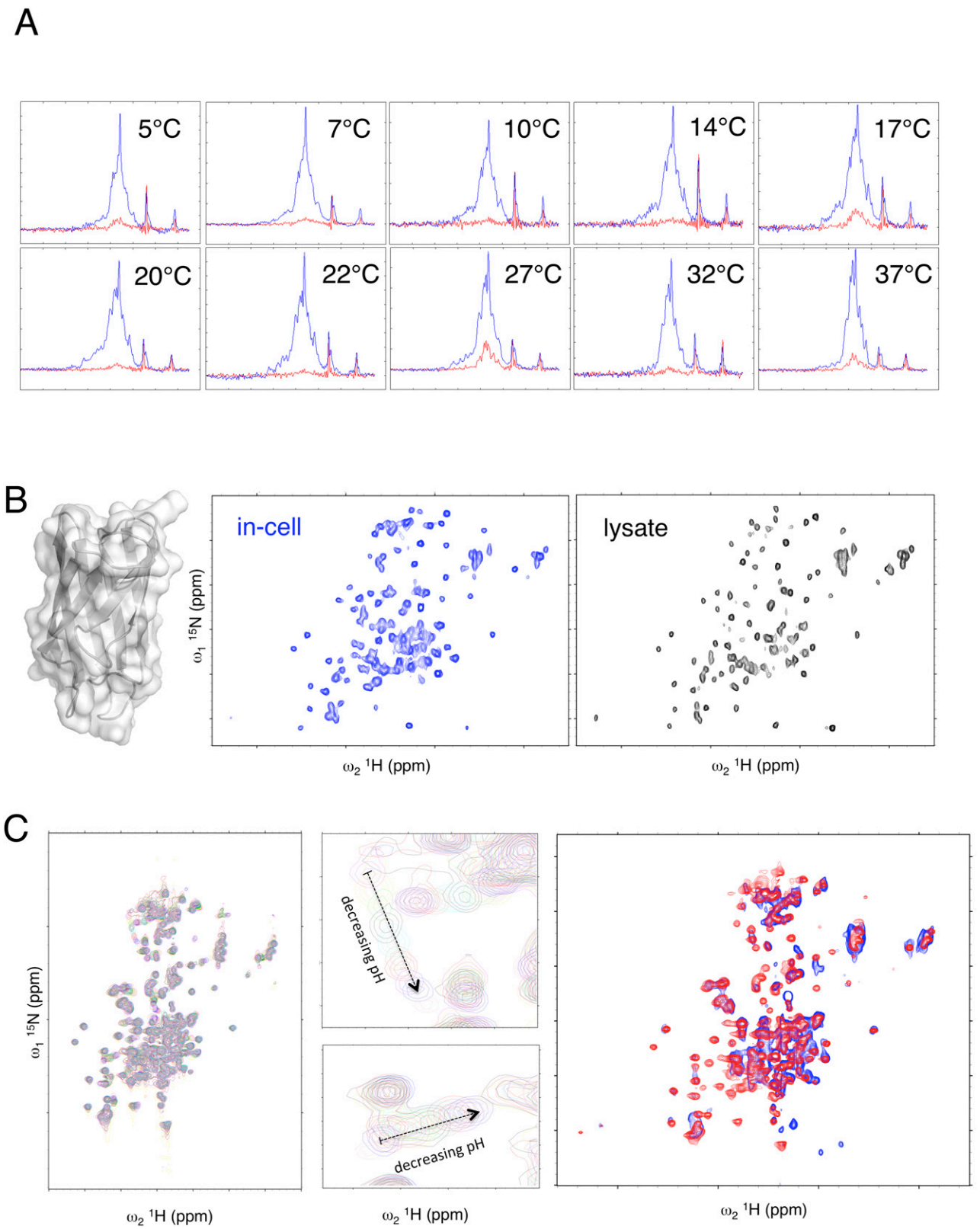

Fig. S2. (*A*) Controls of internalization. One-dimensional ^{15}N-HMQC spectra of SOD1^{I35A} in A2780 cells (blue) and in supernatant (red) show no or small amounts of leakage. (*B*, *Left*) X-ray structure of SOD1^{barrel} (PDB code 4BCZ), representing the β-barrel scaffold of the ALS-associated protein Cu/Zn superoxide dismutase 1 (66). The method yields here intracellular concentrations of 20–30 μM, matching those of human SOD1 in transgenic ALS mice (43) and in vitro aggregation studies (6). (*B*, *Center* and *Right*) HMQC spectra of SOD1^{barrel} in mammalian cells (blue) and the subsequent cell lysate (black). (*C*, *Left*) Overlay of 1H-{^{15}N}-HMQC spectra obtained at pH values ranging from 5.8 to 7.6. (*C*, *Center*) Close-ups of the most affected cross peaks. (*C*, *Right*) Overlay of the best-fit in vitro spectra (red) and the in-cell spectra (blue), used together with the rest of the data to estimate the pH inside the A2780 cells to 6.5 ± 0.1 (32).

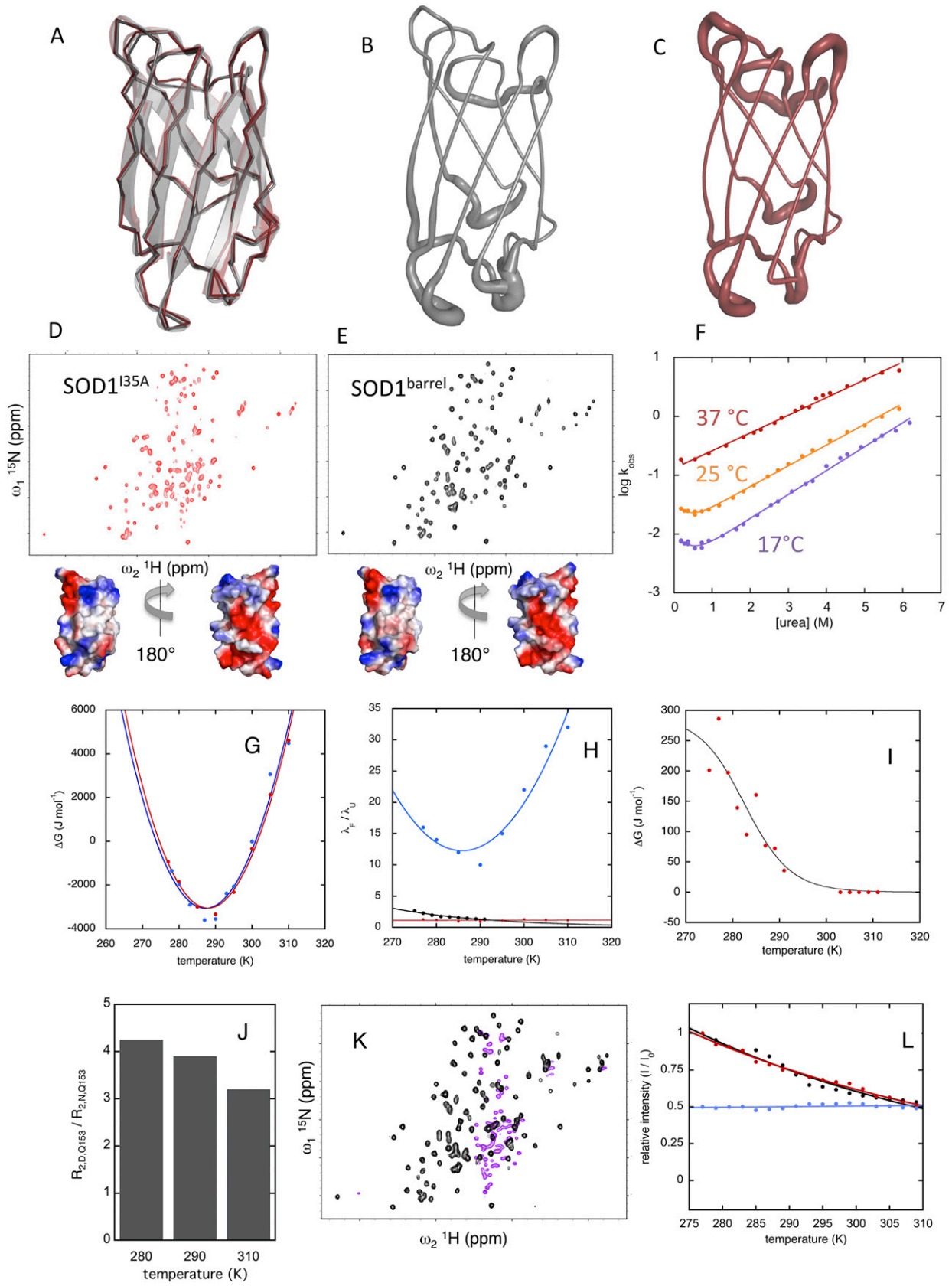

Fig. S3. (*A–C*) The crystal structure of SOD1^{I35A} (PDB code 4XCR) (red) overlaid with that of the SOD1^{barrel} (PDB code 4BCZ) (gray), showing that the folded states of the two protein variants are largely the same. (*D* and *E*, *Upper*) In vitro HMQC spectra of marginally stable SOD1^{I35A} and the fully folded SOD1^{barrel}. (*D* and *E*, *Lower*) The electrostatic surfaces of the two proteins. Taken together, the data show that the structures and surface properties of SOD1^{I35A} and

Legend continued on following page

SOD1^{barrel} are very similar. (*F*) Chevron plots of SOD1^{I35A} at 17 °C, 25 °C, and 37 °C. The lower temperatures show the signature of a two-state folder (28), whereas at 37 °C the midpoint is too low to observe any refolding of the protein. (*G*) The free-energy profile of SOD1^{I35A} in A2780 cells (blue) and in vitro data with a simulated varying selective line broadening of the Q153 cross peak of the folded state, P_F (red). (*H*) The factors of line broadening applied to P_F to reproduce in-cell data (blue) compared with the factors measured from in-cell data (red) and the factors measured in high-viscosity in vitro samples (black). (*I*) Calculated maximum effect on $\Delta G_{D\text{-}N}$ from low-temperature viscosity effects. The peak-volume determination can suffer from systematic errors due to line broadening at low temperatures, but the maximum effect is less than 250 J·mol^{-1}. (*J*) The ratio of R_2 for the folded and unfolded Q153 cross peak at 280 K, 290 K, and 310 K shows only moderate temperature dependence. (*K*) Overlay of HMQC spectra of the folded SOD1^{barrel} and the fully unfolded double-mutant SOD1$^{I35A/G93A}$. (*L*) The relative peak volumes of Q153 D (red) and N (black) as a function of temperature. The calculated population of N remains constant at 0.5 (blue), as expected for a system with only a small contribution from line broadening and relaxation bias.

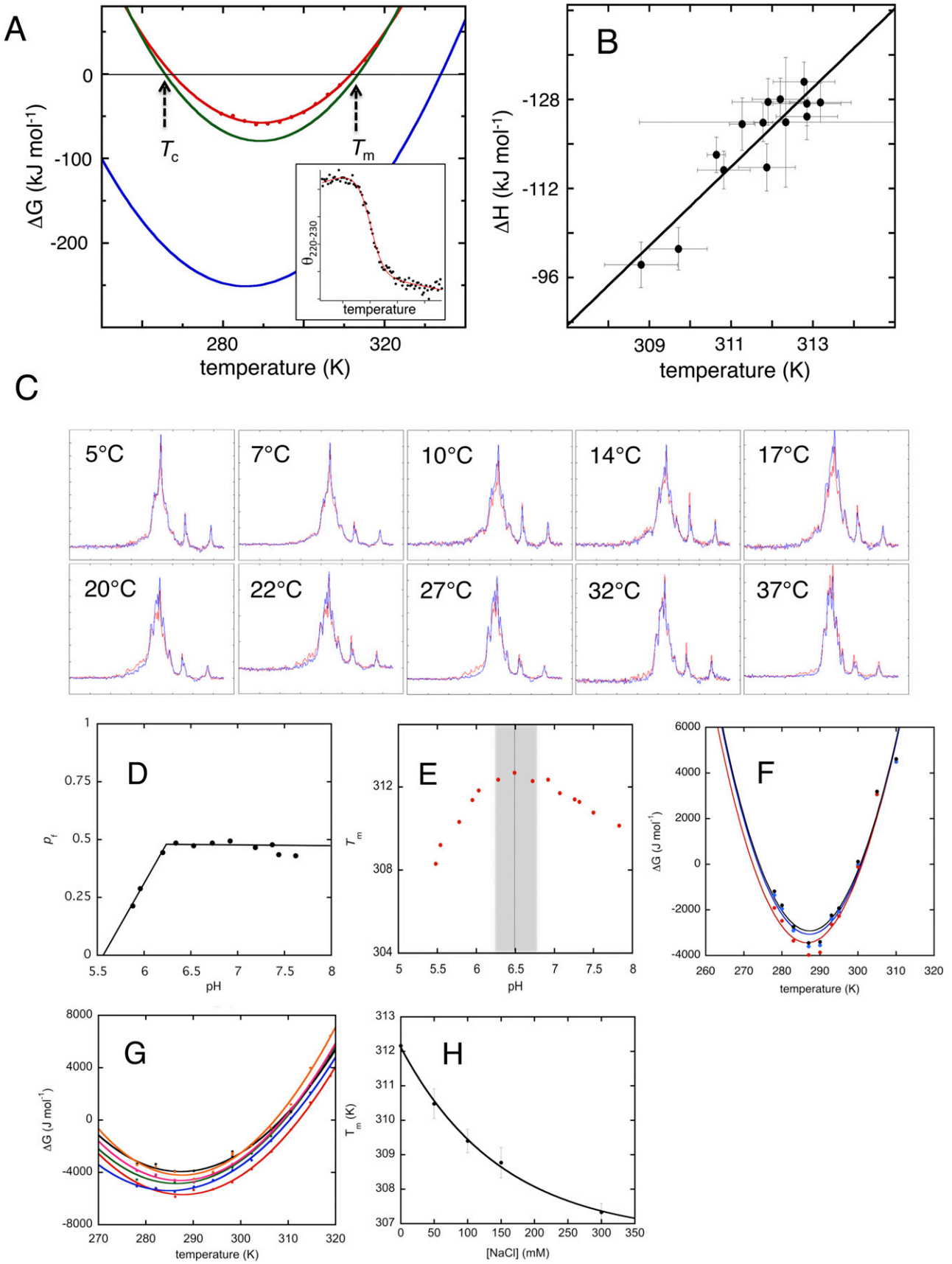

Fig. S4. (*A*) Free-energy profiles of SOD1^{barrel} (blue) and SOD1^{I35A} (green), derived from CD-melting data (*Inset*), compared with the free-energy profile of SOD1^{I35A} determined by NMR (orange). (*B*) The pH dependence of T_m and ΔH of SOD1^{I35A} used to determine ΔC_p from the relationship $\Delta C_p = \delta \Delta H / \delta T_m$.

Legend continued on following page

(*C*) In-cell sample stability vs. time. The 1D 1H-{^{15}N}-HMQC spectra of SOD1^{I35A} in A2780 cells at the start of the experiment (red) and after 2D acquisition (blue) are overall similar. (*D–H*) Controls of pH and salt effects. (*D*) Population folded SOD1^{I35A} material determined from Q153 cross peaks as a function of pH. (*E*) Thermal melting point of SOD1^{I35A} determined by CD as a function of pH. (*F*) Free-energy profiles determined from in-cell data directly (blue) and data skewing arising by offsetting the pH to, 6.25 (red) and 6.72 (black). (*G*) Free-energy profiles for SOD1^{I35A} without added salt (orange) and in increasing amounts of NaCl, up to 300 mM. (*H*) The melting temperatures for SOD1^{I35A} at the NaCl concentrations used in *G*.

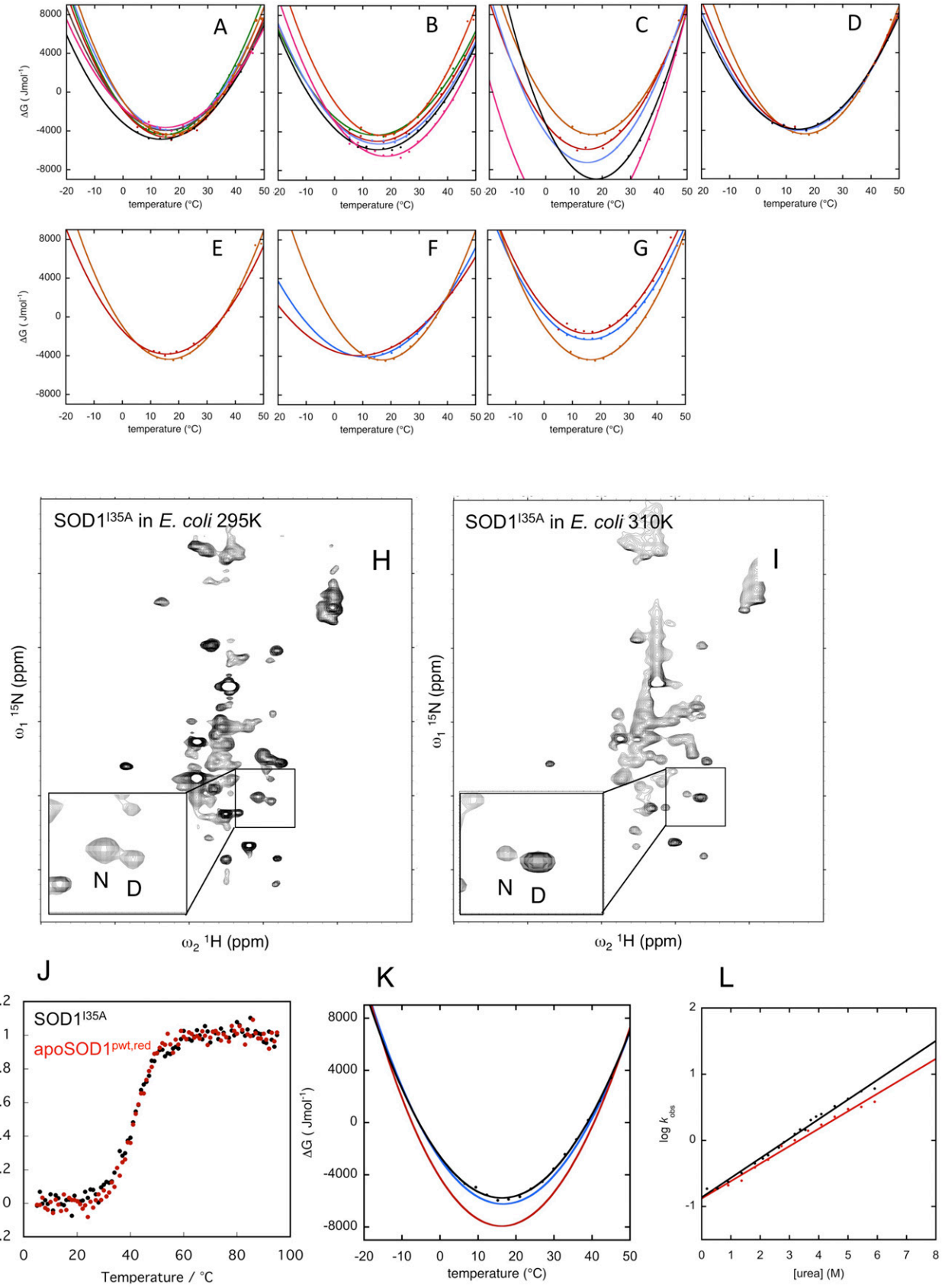

Fig. S5. Free-energy profiles used for in vitro controls. The in vitro references (PBS) are shown in orange. (*A*) The effect of *E. coli* lysates on SOD1^{I35A} stability is critically sensitive to lysate preparation. (*B*) Increasing amounts of the inert crowder Ficoll 70 increases SOD1^{I35A} stability: 50 mg/mL (green), 100 mg/mL (red), 150 mg/mL (blue), 200 mg/mL (black), and 250 mg/mL (pink). (*C*) The corresponding effect of PEG^{400}: 5% (brown), 10% (blue), 20% (black), and 30% (pink).

Legend continued on following page

(*D*) Crowding with BSA yields only moderate effects: 40 mg/mL (red), 80 mg/mL (blue), and 100 mg/mL (black). (*E*) The corresponding effect of 100 mg/mL holoSOD1^{dimer} (red). (*F*) Crowding with TTHA^{pwt}: 50 mg/mL (blue) and 100 mg/mL (red). (*G*) Crowding with lysozyme yields marked destabilization even at low concentrations: 30 mg/mL (blue) and 50 mg/mL (red). (*H* and *I*) In-*E. coli* HMQC spectra of SOD1^{I35A} at 290 K and 310 K show line broadening. Even so, the narrow cross peaks of the dynamic C-terminal Q153 can be used for accurate determination of the D and N populations. (*J*–*L*) Thermodynamic and kinetic similarity of SOD1^{I35A} and reduced apoSOD1^{pwt}. Thermal melting of the two SOD1 variants shows inseparable traces. (*K*) Comparison of free-energy profiles of SOD1^{I35A} derived from NMR (black) and CD data (blue) and the free-energy profile of apoSOD1^{pwt} derived from CD data (red). (*L*) SOD1^{I35A} and reduced apoSOD1^{pwt} show similar unfolding rates and similar linear urea dependence, suggesting similar folded structures (66).

Table S1. Statistics of crystallographic data collection and refinement

Data processing	SOD1^{I35A}
Space Group	P65
Unit cell, Å	a, 70.82; b, 70.82; c, 70.01
Unit cell, °	α, 90.00; β, 90.00; γ, 120.00
Wavelength, Å	1.000
Resolution range, Å	46.1–3.60 (3.94–3.60)
Measured reflections	11,303 (2,754)
Unique reflections	2,203 (533)
Asymmetric unit contents	Dimer
Completeness, %	92.8 (93.8)
Multiplicity	5.1 (5.2)
Mean (*I*) half-set correlation CC(1/2)	0.897 (0.572)
R_{pim} (all *I*+ and *I*–)	0.162 (0.331)
Refinement statistics	
Resolution range, Å	46.1–3.60 (4.53–3.60)
R_{work}	0.185 (0.189)
R_{free}	0.239 (0.236)
No. atoms, protein	1,542
rmsd bond lengths, Å	0.004
rmsd bond angles, °	0.780
Mean B value, Å^2	61.7
Ramachandran plot	
Residues in most favored regions, %	90.74
Residues in allowed regions, %	8.33
Residues in disallowed regions, %	0.93

Values in parentheses are for the highest-resolution shell. $R_{work} = \Sigma||F_{obs}|-|F_{calc}||/\Sigma F_{obs}$, where F_{calc} is the calculated protein structure factor from the atomic model (R_{free} was calculated with 9.97% of the reflections selected).

Table S2. Thermodynamic parameters of the in-cell data and in vitro controls

Protein/conditions	$\Delta G_{D\text{-}N}$*, kJ/mol	ΔC_p*, kJ/mol K	$\Delta H_{D\text{-}N}^{\dagger}$, kJ/mol	$\Delta S_{D\text{-}N}^{\dagger}$, J/mol K	T_m, °C	$T_C^{\ddagger}$, °C	$\delta T_m/\delta c^{\S}$, 10^{-3} K·L·g^{-1}
SOD1^{barrel}/PBS¶	−18.6 ± 0.3	−6.49 ± 0.2	−182.8 ± 2.8	−530 ± 10	61.0 ± 0.3	−33.1 ± 1.8	—
SOD1^{I35A}/PBS	0.64 ± 0.12	−6.96 ± 0.40	−138.8 ± 4.5	−453 ± 14	35.6 ± 0.3	−2.1 ± 1.4	—
SOD1^{I35A}/in A2780 cells	4.49 ± 0.50	−9.54 ± 1.20	−134.0 ± 12.3	−445 ± 34	28.0 ± 0.5	1.1 ± 0.6	—
SOD1^{I35A}/in *E. coli* cells	2.25 ± 0.30	−7.91 ± 1.30	−90.7 ± 11.7	−298 ± 38	31.0 ± 0.7	8.4 ± 1.7	—
SOD1^{I35A}/ficoll 70$^{\#}$	−0.62 ± 0.14	−5.40 ± 0.43	−131.2 ± 6.0	−421 ± 19	38.5 ± 0.4	−7.8 ± 1.7	28 ± 2
SOD1^{I35A}/PEG$^{400\#}$	−0.39 ± 0.15	−8.12 ± 1.55	−194.0 ± 9.4	−624 ± 30	37.6 ± 0.2	−8.3 ± 7.2	22 ± 2
SOD1^{I35A}/holoSOD1$^{dimer\#}$	0.53 ± 0.14	−5.65 ± 0.46	−117.0 ± 5.6	−379 ± 18	35.6 ± 0.4	−4.0 ± 1.8	0
SOD1^{I35A}/BSA$^{\#}$	0.94 ± 0.14	−5.43 ± 0.43	−115.6 ± 5.4	−376 ± 17	34.6 ± 0.4	−6.1 ± 1.8	−8 ± 4
SOD1^{I35A}/TTHA$^{pwt\#}$	1.02 ± 0.13	−3.64 ± 0.42	−92.8 ± 4.7	−303 ± 15	34.0 ± 0.4	−14.8 ± 3.3	−16 ± 6
SOD1^{I35A}/lysozyme$^{‖}$	5.72 ± 0.29	−7.00 ± 1.07	−82.1 ± 5.1	−272 ± 16	21.2 ± 1.0	13.5 ± 2.6	−155 ± 7

*At 37 °C (*SI Materials and Methods*).
†At T_m.
‡Negative values extrapolated from thermodynamic parameters (*SI Materials and Methods*).
§Derived from linear fits of T_m vs. [crowding agent] (Fig. 3).
¶At 37 °C, derived from CD data (*SI Controls*).
$^{\#}$At 37 °C, calculated at 100 mg/mL crowder concentration (*SI Controls*).
$^{‖}$At 37 °C, parameters extrapolated to 100 mg/mL (*SI Controls*).

Table S3. Net charge at pH 6.5 for the proteins used in this study

Protein	Net charge at pH 6.5, e*
BSA	−8.5
$TTHA^{pwt}$	−1.5
$holoSOD1^{dimer†}$	−5
Lysozyme	+8.5
$SOD1^{I35A}$	−0.5

*Calculated as $\sum N_{K,R} - \sum N_{D,E} + (1/2)\sum N_H$, where N_X is the number of residue X. The pK_a value of the histidine side chain is set to 6.5.
†Each $holoSOD1^{dimer}$ coordinate, 2 Cu^{2+} and 2 Zn^{2+}, and the metal ion charge are included in the net charge. The coordinating histidine charge is set to 0, whereas the buried H43 is set to 1.